UCLA
UCLA Previously Published Works

Title

A systematic method for tuning the dynamics of electrostatically actuated vibratory gyros

Permalink

https://escholarship.org/uc/item/6f7707t9

Journal

IEEE Transactions on Control Systems Technology, 14(1)

ISSN

1063-6536

Authors

Kim, DJ

M'Closkey, RT

Publication Date

2006

DOI

10.1109/TCST.2005.860525

Peer reviewed

A systematic method for tuning the dynamics of electrostatically actuated vibratory gyros.

Dong-Joon Kim[1], Robert M'Closkey[2], *Member*

Abstract— **High performance vibratory gyroscopes require two degenerate modal frequencies for maximizing the rate-induced signals relative to noise produced by signal conditioning electronics. The present work introduces a systematic approach for tuning these modes in vibratory gyros that employ electrostatic actuation. The key contribution is recognizing that a parametric model which captures the dependence of the sensor dynamics on the bias electrodes' potentials can be fit to empirical frequency response data via a semidefinite program. The models typically have twenty to thirty parameters for which the frequency response data imposes up to several hundred constraints. Analysis of the identified model enables the direct computation of the bias potentials which yield degenerate modal frequencies. The results are illustrated on a JPL-Boeing MEMS gyro prototype.**

NOMENCLATURE

$\mathbf{C}^{n \times m}$	$n \times m$ matrices with complex elements
$C, \tilde{C}$	positive definite damping matrices
H_{in}	signal conditioning dynamics reflected to the sensor's input
H_{out}	signal conditioning dynamics reflected to the sensor's output
I	identity matrix
j	$\sqrt{-1}$
$K_0, \tilde{K}_0$	positive definite mechanical stiffness matrices
$K_p, \tilde{K}_p$	electrostatic stiffness matrices, $p \geq 1$
Q	quality factor
$M, \tilde{M}$	positive definite mass matrices
n_e	number of bias electrodes
P^*	conjugate transpose of matrix P
$\mathbf{R}^{n \times m}$	$n \times m$ matrices with real elements
s	Laplace transform variable
$\delta v_{k,p}$	potential of $v_{p,k}$ relative to electronic ground
Δ_ω	modal frequency split
μ	normalized frequency detuning parameter
$v_{k,p}$	pth electrode potential during kth experiment
v_{max}	maximum value of electrode potential
$\psi_{k,q}$	empirical frequency response data point at $\omega_{k,q}$
$\bar{\sigma}$	maximum singular value
$\omega_{k,q}$	qth frequency associated with kth experiment

I. INTRODUCTION

The advent of MEMS technologies has facilitated the development of miniaturized, low cost micromechanical vibrating

[1]Graduate Student Researcher

[2]Corresponding Author. Associate Professor, Mechanical and Aerospace Engineering Department, University of California, Los Angeles 90095-1597. rtm@obsidian.seas.ucla.edu.

sensors. Manufacturing imperfections and process variations, however, often make the resonant frequency of the sensor deviate from the design values. Thus, post-fabrication frequency tuning is essential for optimizing sensor performance and various tuning methods have been developed and reported. For example, selectively adding material to the vibrating structure [7] or removing material from the structure [17] can permanently alter the sensor's dynamics. Alternatively, electrothermal tuning can induce changes in resonance by thermally modifying internal stresses [16], [14]. By far the most commonly employed technique is electrostatic tuning which operates by applying DC bias potentials, relative to the sensor's vibrating structure, with the subsequent effect of modifying its stiffness. This approach has found a wide range of applications in single resonator sensors due to its simple implementation [1], [19], [13], [11], [3].

Nowhere is resonance tuning more critical –and challenging –than in vibratory angular rate sensors or "vibratory gyros". In this class of sensors it is necessary to match *two* modal frequencies in order to maximize the signal-to-noise ratio (SNR) associated with the angular-rate-induced signals. Indeed, the *reduction* in SNR when the modes are detuned is given by

$$10\log(1 + 4Q^2\mu^2) \text{ dB,}$$

where Q is the quality factor of the modes, and $\mu = \Delta_\omega/\omega_0$ is the normalized detuning factor corresponding to a modal frequency split of Δ_ω with a nominal modal frequency of ω_0. For example, $Q > 40,000$ and $\omega_0 \approx 4.4kHz$ for the sensor tested in this paper and so the SNR will suffer a decrease of 25 dB from its maximum possible value if the modes are detuned by only 1 Hz.

Our focus is on gyros that employ dedicated electrodes for electrostatic tuning and one of the difficulties in tuning two modes is the coupling that exists between these modes and the bias electrode frame which prevents the selective modification of a single mode without perturbing the second mode. Furthermore, first principles models, for example models based on finite element analysis of the sensor's vibrating structure, are useful for defining a potential model structure but they have limited utility for frequency tuning because one cannot hope to accurately specify the details of the anisoelasticity or anisoinertia that produce the observed detuning associated with a particular device. Thus, a systematic approach for tuning the modes must be based on models derived from experimental data but whose structures are informed by analysis of the sensor mechanics and electronics.

Several research groups have reported the successful application of frequency tuning for their vibratory gyro prototypes,

see [2], [6], [8], [10], [15] for example, however, only [2] provides enough detail to determine the degree of tuning that is actually achieved, and even in this reference it is clear that the SNR can be improved by further reducing Δ_ω. Furthermore, none of these references propose a systematic tuning process which is clearly necessary if these devices are to move beyond the laboratory environment. Our approach for tuning vibratory gyros is to build, from empirical frequency response data, a general two degree-of-freedom sensor model that also includes additional parameters for capturing the features in the test data that are caused by non-colocated sensor-actuator pairs and signal-conditioning electronics. The present paper extends [9] in which a gradient descent algorithm was employed to tune the gyro dynamics. Although the algorithm in [9] proved effective for tuning, it was necessary to perform a large number of frequency response experiments for obtaining descent directions and conducting the line search. The present paper overcomes these inefficiencies by explicitly modeling the dependence of the sensor dynamics on the bias electrode potentials by fitting a single, comprehensive model to multiple frequency response data sets obtained at different bias points. This approach facilitates tuning in essentially "one step." Furthermore, with enough freedom in the bias electrode configuration, it is also possible to satisfy ancillary criteria such as minimizing the maximum required bias voltage or tuning to specific target frequencies. The proposed tuning algorithm has been successfully applied to several MEMS gyro technolgies including the JPL-Boeing microgyro and post-resonator gyro [2], although only the former is discussed in this paper due to space constraints.

II. TUNING ALGORITHM

A. Sensor models

The linear mechanics of tuned vibratory gyros can be captured by the following two degree-of-freedom second order model in a neighborhood of the two resonances that are exploited in angular rate sensing

$$M\ddot{x} + C\dot{x} + \Omega S\dot{x} + Kx = u. \tag{1}$$

In this model M, C, and K are real 2×2 positive definite mass, damping and stiffness matrices, respectively. The angular rotation rate of the sensor is denoted Ω and S is a skew-symmetric matrix that reflects the Coriolis coupling between the two modes since the generalized coordinates are written with respect to a sensor-fixed frame. The stiffness matrix is in fact comprised of an elastic stiffness matrix plus an electrostatic stiffness matrices induced by differential voltage potentials existing between the sensor's vibrating structure and fixed electrodes. The dependence of the total stiffness matrix on the electrode potentials will be made more explicit below.

It is often forgotten that (1) implies that the sensing pick-offs and actuators are collocated. This is most often *not* the case in actual devices where the sensing and actuation electrodes are distributed over different areas of the vibrating structure. Thus, (1) must be embellished in order to model the effects of sensor-actuator non-collocation. Furthermore, most analysis in the literature make various assumptions concerning the system

matrices such as scalar-times-identity mass and damping matrices. We make no such restrictions other than to assume that additional resonances in the sensor's structure are sufficiently far from the modes of interest as to have a negligible effect on the sensor's response in the frequency band of interest and so a general two degree of freedom model like (1) accurately captures the sensor mechanics. The spectral separation of the modes of interest from other potentially interfering modes is addressed as sensor design issue and Fig. 2 demonstrates that this requirement is satisfied for the sensor tested in this paper.

We also assume that additional dynamic elements not associated with the sensor mechanics but that nevertheless contribute features to test data may be entirely reflected to either the sensor's output, in which case they are denoted H_{out}, or to the sensor's input, in which case they are denoted H_{in}. These elements can include the filtering effects of pick-off signal conditioning circuitry, buffering or smoothing circuits on the actuation electrodes, and anti-aliasing filters associated with the data acquisition equipment.

High performance vibratory gyros require at least two sensing pick-offs and two actuators for measurement and stimulation as a consequence of their closed-loop operation. Thus, assuming a two-input, two-output configuration with additional dynamics reflected to the sensor output, the following model is assumed to produce the test data

$$H_{\text{out}}(s)RZ_{\text{act}}^{-1}(s), \tag{2}$$

where s is the Laplace transform variable and

$$Z_{\text{act}}(s) := Ms^2 + Cs + K_0 + \sum_{p=1}^{n_e} K_p v_p^2, \quad R \in \mathbf{R}^{2 \times 2}.$$

This model uses as its basis the updated version of (1)

$$M\ddot{x} + C\dot{x} + \left(K_0 + \sum_{p=1}^{n_e} K_p v_p^2\right)x = u$$
$$y = Rx, \tag{3}$$

where the stiffness matrix has been explicitly decomposed into the sum of a positive definite *mechanical* stiffness matrix, denoted K_0, and n_e negative-semidefinite *electrostatic* stiffness matrices, denoted K_p, $p = 1, \ldots, n_e$, that are associated with the corresponding bias electrode potentials v_p, $p = 1, \ldots, n_e$. The quadratic appearance of the bias potentials and the fact that $K_p \leq 0$ can be motivated by analysis of the energy stored in the capacitors created by the bias electrodes and sensor structure, however, these details will not be pursued in this paper.

The output y in (3) represents the 2×1 vector of displacements measured at the pick-offs, and u represents the 2×1 net actuator forces applied to the structure. The form of (3) assumes that the x variable is defined by the frame established by the actuators –hence the subscript in Z_{act}. In other words, x represents a signal that is proportional to the position of the sensor's vibrating structure at the actuator electrodes. Thus, R is a nonsingular matrix that transforms the displacements at the actuators into displacements at the sense pick-offs and hence models the effects of sensor-actuator non-collocation or

even differently sized pick-off electrodes. Furthermore, (3) implies that the actuator electrodes are identical in the sense that the same potential applied to each electrode produces forces of equal magnitudes. This is not an overly restrictive assumption given that many MEMS gyros are fabricated with a high degree of symmetry in the electrode layout (see Fig. 1). Any dynamics and signal conversion constants associated with the voltage-to-force or displacement-to-voltage conversion process are assumed to be captured by H_{out}.

An analogous model for describing the observed data may be developed from the point of view of writing the equations of motion with coordinates established by the pick-off electrodes. In this case, however, we assume that the effects of any additional dynamic elements can be reflected to the sensor's *input* as H_{in}. Thus, we assume the observations to be generated by the following alternative model,

$$Z_{\text{sen}}^{-1}(s)BH_{\text{in}}(s), \tag{4}$$

where

$$Z_{\text{sen}}(s) := \tilde{M}s^2 + \tilde{C}s + \tilde{K}_0 + \sum_{p=1}^{n_e} \tilde{K}_p v_p^2, \quad B \in \mathbf{R}^{2\times 2}.$$

In direct analogy with using (3) to define Z_{act}, (5) is used to define Z_{sens},

$$\tilde{M}\ddot{z} + \tilde{C}\dot{z} + \left(\tilde{K}_0 + \sum_{p=1}^{n_e} \tilde{K}_p v_p^2 \right) z = Bu$$
$$y = z, \tag{5}$$

where the z variable is defined by the sense pick-off frame, and where B captures, among other things, the effects of non-collocated sense pick-offs and actuator electrodes. The system matrices in (5) are in general different than those in (3), however, when the damping matrix is positive definite, as it is in any practical application, these two descriptions are equivalent and the x and z variables are related by a unique transformation. Thus, it is possible to model the sensor, in the case with additional dynamics at the output, as $H_{\text{out}}Z_{\text{sen}}^{-1}B$ but it will become clear in Section II-D why we wish to associate (3) with H_{out} and (5) with H_{in} thereby yielding the model choices (2) and (4).

B. Frequency response data

The parameters in (3) or (5) will be determined by fitting the appropriate model to two-input/two-output frequency response data sets acquired from multiple experiments. The kth frequency response data set is generated with the fixed bias electrode potentials $\{1, v_{k,1}, v_{k,2}, \ldots, v_{k,n_e}\}$, where the first element is fixed to 1 and represents a fictitious potential associated with the mechanical stiffness matrix K_0. The additional subscript in v is used to identify the experiment. If n_{exp} experiments are conducted, it is clear from the additive nature of the mechanical and electrostatic stiffness matrices in (3) and (5) that

$$\text{rank} \begin{bmatrix} 1 & v_{1,1}^2 & v_{1,2}^2 & \cdots & v_{1,n_e}^2 \\ 1 & v_{2,1}^2 & v_{2,2}^2 & \cdots & v_{2,n_e}^2 \\ \vdots & \vdots & \vdots & \ddots & \vdots \\ 1 & v_{n_{exp},1}^2 & v_{n_{exp},2}^2 & \cdots & v_{n_{exp},n_e}^2 \end{bmatrix} = n_e + 1 \tag{6}$$

is necessary and sufficient for uniquely identifying $K_0, K_1, \ldots, K_{n_e}$. Hence, at least $n_e + 1$ frequency response experiments must be conducted.

Lastly, we assume the kth frequency response experiment yields m_k frequency response data points $\{\psi_{k,1}, \psi_{k,2}, \ldots, \psi_{k,m_k}\}$, $\psi_{k,q} \in \mathbf{C}^{2\times 2}$, corresponding to the frequencies $\{\omega_{k,1}, \omega_{k,2}, \ldots, \omega_{k,m_k}\}$.

C. Objective Function

The minimax optimization problem for estimating the parameters in (3) is

$$\min_{\substack{M>I, C>0 \\ K_p \leq 0, p=1,\ldots,n_e \\ K_0 + \sum K_p v_p^2 > 0 \\ R_l \in \mathbf{C}^{2\times 2}, l=0,1,\ldots,n_R}} \max_{\substack{k=1,\ldots,n_{\exp} \\ q=1,\ldots,m_k}} \bar{\sigma}\left(\tilde{R}_{k,q} - \psi_{k,q}Z_{\text{act}}(j\omega_{k,q}) \right), \tag{7}$$

where

$$\tilde{R}_{k,q} := \sum_{l=0}^{n_R} R_l \omega_{k,q}^l,$$

and where evaluating Z_{act} at the qth frequency point associated with the kth experiment yields

$$Z_{\text{act}}(j\omega_{k,q}) := -M\omega_{k,q}^2 + K_0 + \sum_{p=1}^{n_e} K_p v_{k,p}^2 + jC\omega_{k,q}.$$

The $M > I$ constraint in (7) is imposed rather than the typical $M > 0$ because in the latter case all of the free parameters may scaled by an nonzero constant so as to make the cost arbitrarily small without actually changing the model frequency response.

The model parameters are obtained by recasting (7) as the following convex optimization problem

$$\begin{aligned} \text{min:} \quad & \gamma \\ \text{subject to:} \quad & J_{k,q} > 0, k = 1, \ldots, n_{\exp}, q = 1, \ldots, m_k \\ & M > I, C > 0, K_0 + \sum K_p v_p^2 > 0 \\ & K_p \leq 0, p = 1, \ldots, n_e, \\ & R_l \in \mathbf{C}^{2\times 2}, l = 0, \ldots, n_R \end{aligned} \tag{8}$$

where

$$J_{k,q} := \begin{bmatrix} \gamma I & \left(\tilde{R}_{k,q} - \psi_{k,q}Z_{\text{act}}(j\omega_{k,q}) \right)^* \\ \tilde{R}_{k,q} - \psi_{k,q}Z_{\text{act}}(j\omega_{k,q}) & \gamma I \end{bmatrix}.$$

There are several commercially available software tools for solving (8). An analogous optimization problem can be formulated to solve (10).

A more natural formulation of the problem would suggest replacing the objective of (7) with

$$\bar{\sigma}\left(H_{\text{out}}RZ_{\text{act}}^{-1}(j\omega_{k,q}) - \psi_{k,q} \right), \tag{9}$$

which minimizes the largest frequency response error of (2). This formulation, however, places too much emphasis on reducing the modeling error at those frequencies and "directions" where $\bar{\sigma}(\psi)$ is relatively large and thereby produces poor fits elsewhere. The frequency response data presented in Section III spans almost four order of magnitude in a very narrow frequency band so this issue is quite relevant and we have found

that the objective in (7) provides superior matching between the identified model frequency response and empirical data.

Another difference between (7) and (9) is that $H_{\text{out}}R$ has been replaced by $\tilde{R}$. This recognizes the fact that any additional dynamics due to, for example, signal conditioning preamplifiers should not exhibit significant magnitude and phase changes in a neighborhood of the resonant modes we are modeling with (3). If these dynamics can be reflected to the sensor output then they can be *combined* with R into a low order polynomial function of frequency with coefficients in $\mathbf{C}^{2\times 2}$, i.e. $\tilde{R}$ is degree n_R. In fact, $\tilde{R}$ can be viewed as combining the first few terms of the Taylor series expansion of the frequency response function of H_{out} with sensor-actuator non-collocation effects. This last point reveals the motivation for writing the equations of motion as they appear in (3) when additional dynamics can be reflected at the sensor output: the argument of $\bar{\sigma}$ in (7) remains an affine function of the decision variables.

A similar development can be made when the effects of any additional dynamics can be reflected to the sensor input as H_{in}. In this case the minimax problem becomes

$$\min_{\substack{\tilde{M}>I,\tilde{C}>0 \\ \tilde{K}_p\leq 0,\, p=1,\ldots,n_e \\ \tilde{K}_0+\sum \tilde{K}_p v_p^2>0 \\ B_l\in\mathbf{C}^{2\times 2},\, l=0,1,\ldots,n_B}} \max_{\substack{k=1,\ldots,n_{\text{exp}} \\ q=1,\ldots,m_k}} \bar{\sigma}\left(\tilde{B}_{k,q}-Z_{\text{sen}}(j\omega_{k,q})\psi_{k,q}\right), \quad (10)$$

where

$$\tilde{B}_{k,q} := \sum_{l=0}^{n_B} B_l \omega_{k,q}^l, \text{ and}$$

$$Z_{\text{sen}}(j\omega_{k,q}) := -\tilde{M}\omega_{k,q}^2 + \tilde{K}_0 + \sum_{p=1}^{n_e} \tilde{K}_p v_{k,p}^2 + j\tilde{C}\omega_{k,q}.$$

In this case, the sensor dynamics are written according to (5) so that BH_{in} in (4) can be modeled as $\tilde{B}$.

D. Tuning algorithm

The tuning algorithm is simply stated:

1) Perform n_{exp} frequency response experiments that satisfy (6),
2) Estimate $\{M,C,K_0,\ldots,K_{n_e},R_0,\ldots,R_{n_R}\}$ from (8),
3) Select v_p so that the generalized eigenvalues of

$$\lambda M - \left(K_0 + \sum_{p=1}^{n_e} K_p v_p^2\right)$$

   are equal, i.e. the modal frequencies are *tuned*. There exist numerous methods for effectively solving this problem because $n_e < 10$, typically. There may be additional degrees of freedom that permit the specification of additional criteria such as tuning the modal frequencies to a specific frequency target or minimizing the magnitudes of the bias potentials.
4) From the point of view of the identified model, the algorithm terminates at Step 3, however, in practice it is prudent to conduct a frequency response experiment with bias voltages from Step 3 to verify that the modal frequency split, Δ_ω, is less than some acceptance criteria. If

the acceptance criteria is exceeded then it is necessary to return to Step 1.

We give several examples for estimating the bias potentials under different tuning criteria in Section III.

III. APPLICATION TO JPL-BOEING MEMS GYROS

The tuning algorithm presented in Section II-D is applied to a JPL-Boeing MEMS gyro prototype. We demonstrate that the modal frequencies for this particular device, with Q exceeding 40K, can be consistently tuned such that $\Delta_\omega < 10$ mHz. The tuning realizes more than a 40 dB improvement in sensor's signal-to-noise ratio relative to the untuned case.

A. Sensor description

The JPL-Boeing sensor essentially consists of a thin cloverleaf-shaped plate with vertical post suspended above a baseplate with eight electrodes as shown in Fig. 1. Two electrodes, commonly termed the sensing electrodes, are used to measure the deflection of the cloverleaf structure, and another two electrodes, the driving electrodes, are used for actuation. The sensing pick-off configuration actually gives estimates of velocities at points on the vibrating cloverleaf. The models presented in Section II-A are easily modified for this situation. The remaining electrodes may be used to create bias potentials between the electrodes and cloverleaf thereby altering the dynamics of the sensor. This design provides a large area for capacitive sensing and the vertical post strongly couples the two lightly damped modes corresponding to tilting deflection of the plate. The mechanical elements are hermetically sealed in a high vacuum to reduce damping. The caption of Fig. 1 describes the sensor's electrode configuration for the tests reported in this paper.

The excitations of the sensor's lightly damped modes can be accomplished by applying a potential to the driving electrodes directly from a function generator or digital-to-analog converter (DAC) and the subsequent response is measured by converting the charge on the sense electrodes into a buffered output voltage that is proportional to the rate of change of the gap between the electrodes and the cloverleaf. More detailed information on the design and fabrication of the sensors is provided in [18].

The wide-band MIMO frequency response magnitude of the sensor is shown in Fig. 2. The first lightly damped mode near 2.7 kHz corresponds to the sensor's linear translation mode along the post direction. The next lightly damped mode near 4.4 kHz are actually the two rocking modes of the sensor which are exploited for angular rate detection. In this scale, however, these modes cannot be individually resolved. The remaining lightly damped modes above 5 kHz are other flexural modes of the sensor's elastic structure. The overall positive slope of the frequency response magnitude up to 35 kHz is caused by parasitic capacitive coupling between electrodes, and the attenuation above 35 kHz is caused by preamplifier roll-off. Lastly, the sharp notches near the linear translational mode and the rocking modes are caused by charge cancellation between motion-induced charge and the parasitic capacitance-induced charge. Further information on the wide-band sensor dynamics is provided in [4].
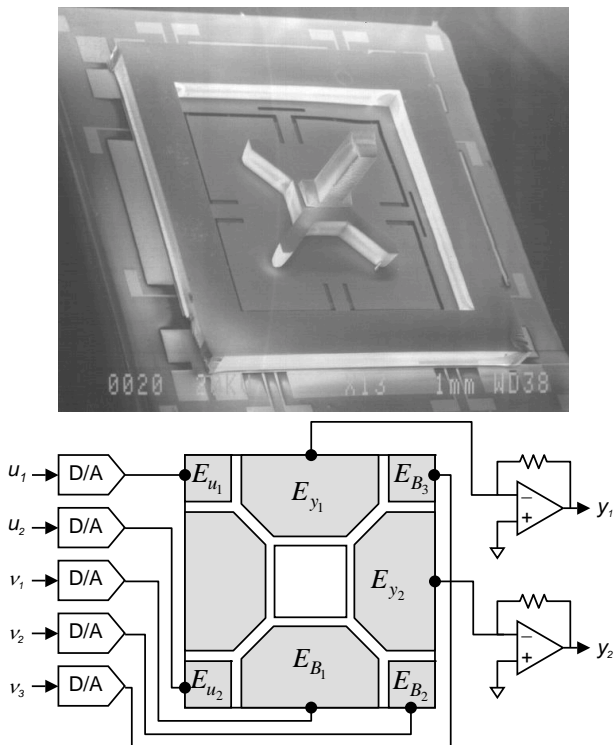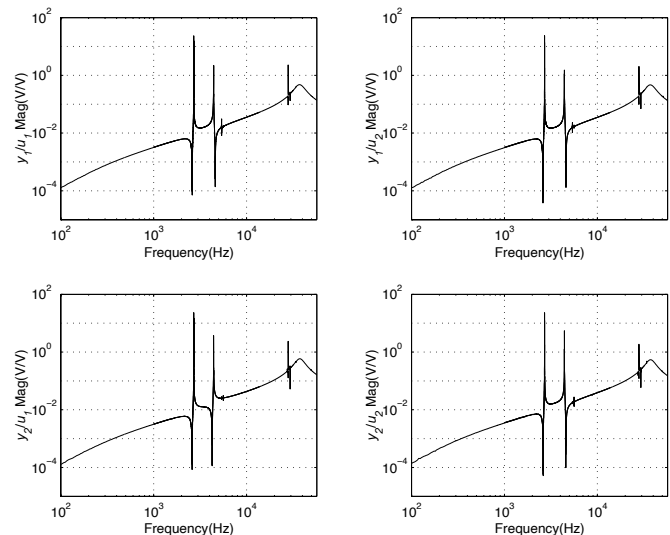
Fig. 2. Wide-band frequency response of the sensor dynamics. The Coriolis-coupled modes are near 4.4 kHz and cannot be resolved on this frequency scale. The other resonances, especially the large resonance near 2.7 kHz, are well-separated from this pair, hence (1) can be used to describe the sensor mechanics in a neighborhood of the 4.4 kHz modes. Parasitic coupling between the actuation electrodes and sensing pick-off is difficult to avoid because of the extremely high gain ($\sim$ 100M) of the transimpedance amplifiers and this produces the trend proportional to frequency in the plots.

Fig. 1. Photo of JPL-Boeing gyro (top) showing the cloverleaf structure that is elastically suspended above a baseplate with an eight electrode layout (bottom schematic). The cloverleaf structure measures about 7mm × 7mm. The "actuators" are the two electrodes labeled E_{u_1} and E_{u_2}, and the sensing pick-offs are the electrodes labeled E_{y_1} and E_{y_2}. The electrostatic tuning electrodes are labeled E_{B_1}, E_{B_2} and E_{B_3}. The sensing and actuation electrodes evidently are not collocated.

The sensor ideally possess two degenerate modal frequencies for the Coriolis-coupled modes since this imparts the largest sensor scale factor (SF), and thereby maximizes the signal-to-noise ratio with respect to electronic noise. Manufacturing imperfections and package-induced stresses, however, always *detune* the modal frequencies. The device tested for this paper features a native frequency split of approximately 5 Hz when all bias potentials are set to the sensor's local electronic ground. Fig. 3 shows the empirical frequency response of the sensor with a frequency resolution of 0.1 Hz in neighborhood of the two Coriolis-coupled modes with the bias potentials at ground. These data are obtained using a closed-loop testing method which provides a rapid assessment of the sensor frequency response over a band encompassing the modes. It is also worth mentioning that the open-loop ARX modeling scheme presented in [12] can locate these modes with sub-hertz resolution so the frequency response testing range is easily determined. The frequency split shown in Fig. 3 would reduce the SF by 40 dB relative to the SF that can be realized when the modes are tuned to degeneracy. Therefore, post-fabrication tuning, preceded by an accurate estimation of the sensor dynamics, is an essential part of optimizing sensor performance.

We now define some modified notation concerning the bias electrode potentials. The sensor's vibrating structure is maintained at a constant potential, denoted v_{gyro}, relative to the electronic ground. The bias electrode potentials, v_k, must be de-fined with respect to v_{gyro}. On the other hand, it is often more convenient to define these potentials relative to the electronic ground. Thus, we define δv_k to be the kth bias electrode's potential relative to ground, i.e. $v_k = v_{\text{gyro}} - \delta v_k$.

B. Tuning results with two electrodes

This section presents extensive results on the algorithm performance when two electrodes ($n_e = 2$) are used for tuning the sensor dynamics. There is good motivation for reflecting additional dynamics to the sensor's output for the tested device because the "actuator" electrode potentials are directly specified by simultaneously-converting DACs whereas the sampled sensor response is first filtered by the signal conditioning buffers associated with the sense pick-off electrodes. Thus, a natural model for these sensors is to include signal-conditioning effects at the sensor's output and to place no additional dynamics at the sensor's input. Note, however, that identical signal conditioning on each measurement or actuator channel can be reflected to the plant input or output since these dynamics commute with those of the sensor mechanics. The difficulty arises when *differential* perturbations are introduced between the channels. Our experimental results indicate a small differential phase of approximately 1 deg. is introduced between the pick-offs by the signal conditioning circuitry. Although this is a small amount of differential phase, we will show that the identified models assuming additional output dynamics provide more accurate results in determining the tuning potentials as compared to models that are identified assuming additional dynamics can be reflected to the sensor input.

We initially report the results of tuning the sensor from its native state when all $\delta v_k = 0$. Three frequency response data
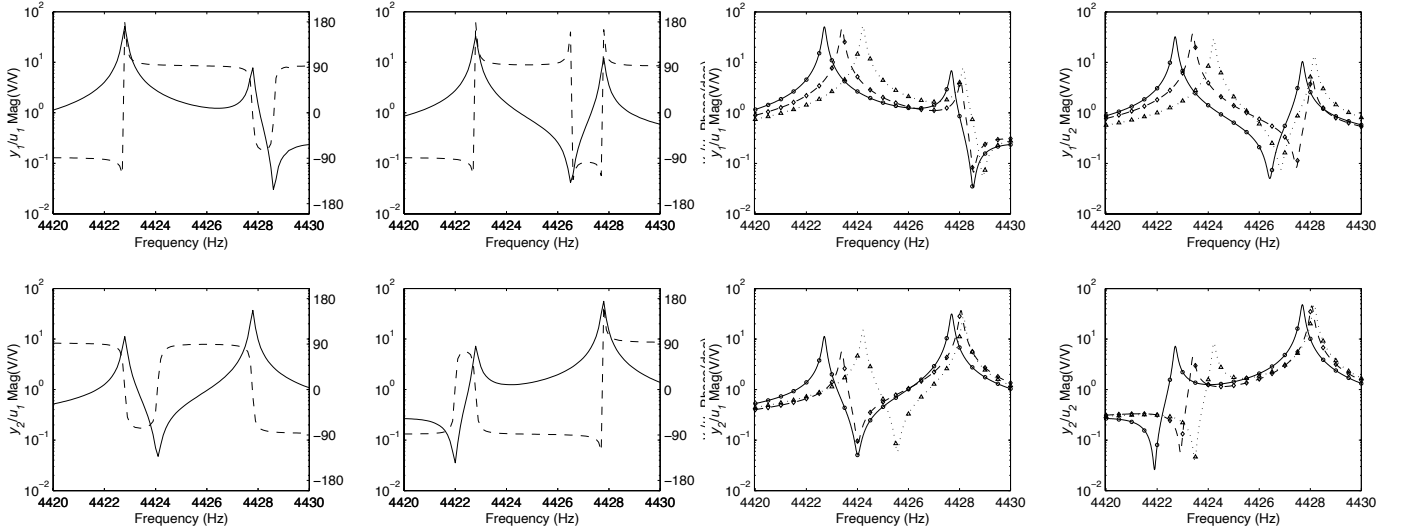
Fig. 3. Empirical frequency response with 0.1 Hz frequency resolution in a neighborhood of the Coriolis-coupled modes –magnitude (solid) and phase (dash). The input rate is zero and all bias electrode potentials are set to the sensor's electronic ground. Thus, these dynamics represent the native, or untuned, state of the sensor. The frequency split between the resonances is $\Delta_\omega \approx 5$ Hz which produces a 40 dB reduction in the sensor's scale factor with a concomitant reduction in the signal-to-noise ratio.

sets ($n_{exp} = 3$) are obtained at the following bias potentials,

$$[\delta v_{1,1}, \delta v_{1,2}] = [0, 0] \tag{11}$$

$$[\delta v_{2,1}, \delta v_{2,2}] = [1, 0] \tag{12}$$

$$[\delta v_{3,1}, \delta v_{3,2}] = [0, 1]. \tag{13}$$

As noted at the end of Section III-A these potentials are stated with respect to the sensor's electronic ground, however, they do satisfy (6). Each data set spans 4385 Hz to 4445 Hz with 0.5 Hz resolution ($m_1 = m_2 = m_3 = 121$). Furthermore, we select $n_R = 1$ so total of 23 parameters are identified from (7). The empirical data and resulting model frequency responses evaluated at (11) thru (13) are shown in Fig. 4. The displayed frequency range is smaller than that of the data used in the computations in order to demonstrate that the model's frequency responses essentially interpolates the data.

Two bias electrodes generically permit the tuning of the modes to degeneracy, however, the tuned frequency cannot be specified. The following optimization yields the bias potentials, if they exist, that tune the modal frequencies to degeneracy with the constraint that the potentials cannot exceed v_{max},

$$\begin{aligned} \text{min:} \quad & \gamma \\ \text{subject to:} \quad & \gamma M - \left(K_0 + \sum_{p=1}^{n_e} K_p v_p^2 \right) \geq 0 \ . \\ & v_{max}^2 \geq v_p^2 \geq 0, \ p = 1, \dots, n_e \end{aligned} \tag{14}$$

The voltage range applied to the bias electrodes is limited by the DA converters to ± 10V, i.e. $v_{max} = 10$, however the sensor can be tuned to degeneracy within these limits. The predicted tuning potentials are

$$[\delta v_1, \delta v_2] = [2.050, 4.380], \tag{15}$$

and the tuned frequency is near 4430 Hz.

Fig. 4. Empirical frequency response of the sensor at the set of biases given in (11) to (13) compared to the frequency response of the model fit to this data by solving (7). Additional dynamics are reflected to sensor's output in this case. The circles, diamonds, and triangles correspond to the data generated at (11), (12), (13), respectively, and conclusively demonstrate that the bias electrode potentials do indeed modify the sensor dynamics since it is quite evident that the resonant frequencies change as do the positions of the zeros. These three data sets are used to explicitly determine the effect of the bias potentials on the sensor dynamics: the solid, dash, and dotted line types are the frequency responses of the identified model evaluated at these bias potentials. Direct tuning of the sensor's dynamics is now possible using this model.

The frequency response of the sensor tested with these applied bias potentials is shown in Fig. 5 along with the frequency response of the original model evaluated at (15) (not a new model fit to this data). The model predicts identical modal frequencies and the data on this scale also suggest that the modes are in fact degenerate. A subsequent frequency response test with 10 mHz frequency resolution, however, illustrates that there is an approximately 15 mHz difference in the modal frequencies: Fig. 6 shows the sensor's empirical frequency response in a 200 mHz band centered about the predicted tuned frequency. This modal frequency difference produces very little degradation in the SNR compared the maximum achievable value so the sensor for all practical purposes is "tuned."

Although we have demonstrated that the sensor has been tuned in one iteration of the algorithm it is necessary to compile statistics concerning the performance of the tuning algorithm starting from different bias electrode potentials to model different native sensor states. This is the focus of the remainder of the section. We assume a "truth" model for these computations by identifying the sensor parameters about the nominal tuning potentials (15) which we know result in a 15 mHz frequency split. This yields the following tuning potentials that are slightly perturbed from (15),

$$[\delta v_1, \delta v_2] = [2.039, 4.401]. \tag{16}$$

This newly identified model is used to determine level sets in the v_1-v_2 plane centered at (16) that represent a given amount of *detuning* between the modes as shown in Figs. 7 thru 10. The following grid of bias electrode potentials

$$\{(\delta v_1, \delta v_2) \,|\, \delta v_k \in [-9, -6, \dots, 6, 9], \ k = 1, 2\}, \tag{17}$$
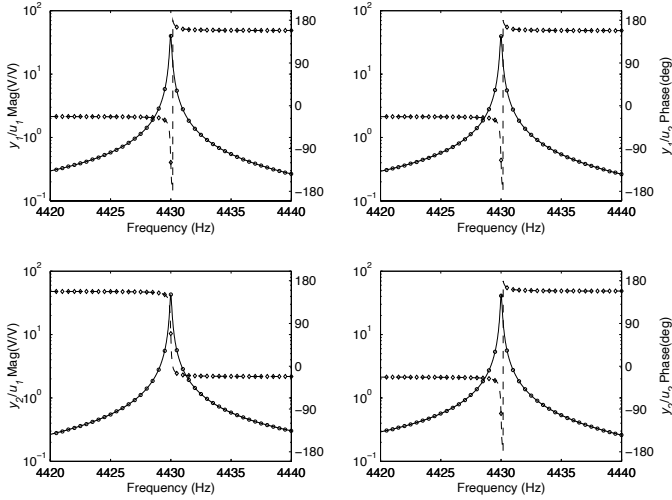
Fig. 5. Empirical frequency response of the sensor (magnitude –circle; phase –diamonds) at the biases predicted to tune the modes to degeneracy, i.e. (15), in addition to the frequency response of the model from Fig. 4 (magnitude –solid; phase –dash) evaluated at these bias potentials. The model's modal frequencies are, of course, equal and the data suggest that the actual modal frequencies must be very close since only a single peak is evident in each channel. This is confirmed in Fig. 6 which displays frequency response data in a 200 mHz neighborhood of the modes.
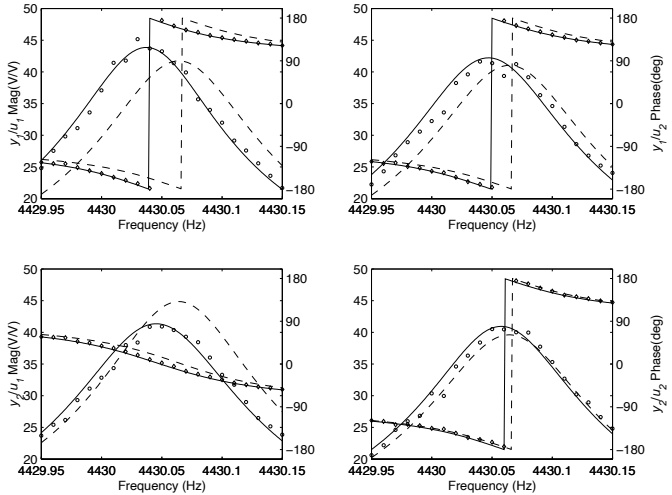
Fig. 6. Empirical frequency response of the sensor with 10 mHz resolution tested at (15) (magnitude -circle; phase -diamond) and compared to the tuned identified model from Fig. 4 (dash trace for both magnitude and phase). The solid trace is a new model fit to the data in this plot and is used to estimate an actual frequency split of approximately 15 mHz.

which corresponds to a total of 49 nominal bias points, were used to compile statistics on the algorithm performance. Three frequency response tests are conducted in association with each of these "starting" bias points and the data from each experiment spans 4385 Hz to 4445 Hz with 0.5 Hz resolution. Thus, for a given $\{\delta v_1, \delta v_2\}$ selected from (17), the following bias vectors are used to collect frequency response data

$$
\begin{aligned}
&[\delta v_1, \delta v_2] \\
&[\delta v_1 + 1, \delta v_2] \\
&[\delta v_1, \delta v_2 + 1].
\end{aligned}
\tag{18}
$$

As was noted earlier, additional dynamics are reflected to the
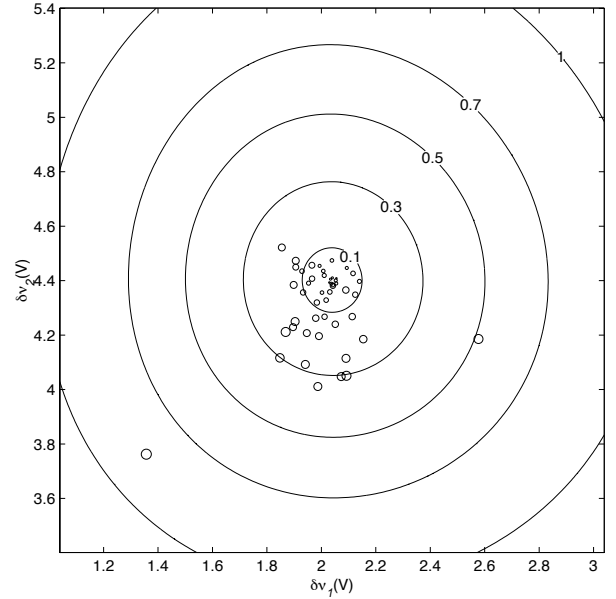

Fig. 7. Results of tuning the sensor dynamics after one iteration of the algorithm with the sensor model that assumes additional dynamics are reflected to its output. The points represent the computed bias electrode potentials that are necessary to tune the modes to degeneracy according the model that is identified at each of the bias points given in (17). Ideally, each identified model would predict the bias potentials to be (16), however, this is not the case. The point diameter is proportional to the norm of the initial bias point minus the biases in (16) so the larger circles represent starting points which are furthest away from (16) and in fact these starting points have the poorest estimate of the bias potentials necessary to tune the sensor. Some of the initial bias points correspond to modal frequency splits of more than 15 Hz. The mean values of the predicted biases are $\bar{\delta} v_1 = 2.005$ and $\bar{\delta} v_2 = 4.311$ and their standard deviations are $\sigma(\delta v_1) = 0.146$ and $\sigma(\delta v_2) = 0.150$. The concentric circles represent estimates of the frequency detuning Δ_ω (in Hertz) obtained from a model fit to data generated at (16).

sensor output and so the 23 model parameters are identified from (7) with $n_{\exp} = 3$, $m_1 = m_2 = m_3 = 121$ and $n_R = 1$. The subsequent model is used to compute its associated tuning biases and these are plotted in Fig. 7. All 49 starting bias points are represented in this figure and the size of the circle is proportional to the norm of the difference between the starting biases taken from (17) and the assumed tuning values (16). As would be expected, the larger circles, which are associated with starting biases furthest from (16), yield the poorest estimates of (16). The majority of the estimates, however, tune the modes such that $\Delta_\omega < 300$ mHz. At this point a second tuning iteration is performed and the these results are shown in Fig. 8. At the termination of the second tuning step all cases with the exception of one are tuned such that $\Delta_\omega < 10$ mHz.

It is informative to apply the algorithm when additional dynamics are referred to the sensor's input as a means of illustrating the impact of model choice on algorithm performance. In this case (10) is used for the sensor model and we generate results analogous to Figs. 7 and 8. Starting with the same initial bias points represented in (17) the algorithm yields the tuning results shown in Fig. 9 after the first iteration. It is clear from this figure that the model assuming input dynamics yields inferior predictions of the tuning potentials. A second iteration shown in Fig. 10, however, essentially tunes the modes to the same degree as the model with additional output dynamics.
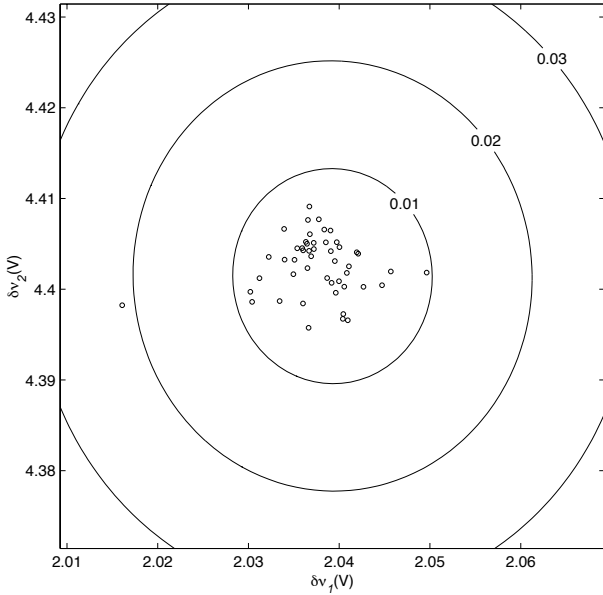
Fig. 8. The results of a second iteration of the algorithm in which new models are identified at the biases represented in Fig. 7. All cases are tuned to within 10 mHz with the exception of one case for which $\Delta_\omega = 20$ mHz.
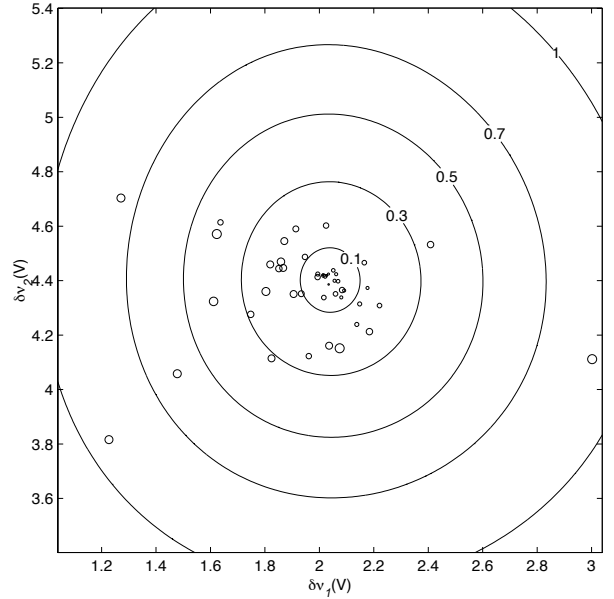

Fig. 9. Results of tuning the sensor dynamics after one iteration of the algorithm with a sensor model that assumes additional dynamics are reflected to its input. The points represent the computed bias electrode potentials that are necessary to tune the modes to degeneracy according the model that is identified at each of the bias points given in (17). The mean values of the predicted biases are $\bar{\delta v}_1 = 2.071$ and $\bar{\delta v}_2 = 4.241$ and their standard deviations are $\sigma(\delta v_1) = 0.762$ and $\sigma(\delta v_2) = 0.669$. This figure reveals that the model assuming additional dynamics reflected to the sensor's input does not perform as well as the model assuming dynamics at the sensor's output, cf. Fig. 7.

This is not surprising because Z_{sen} and Z_{act} are nearly scalar-times-identity transfer functions, in so far as the damping is classical, once the first iteration is complete. Hence, input dynamics will commute with Z_{sen} to produce equivalent dynamics at the plant output and visa versa. Although one cannot predict which model will yield better estimates of the tuning potentials without extensive testing, which would defeat the purpose of an efficient tuning algorithm, we argued at the beginning of this section that additional output dynamics are most appropriate for this sensor based on its signal conditioning configuration and this is consistent with the identification results.

C. Tuning results with three electrodes

Tuning results using three bias electrodes are briefly described in this section. Tuning from the native sensor state in which $\delta v_k = 0$ is the only case we address. An additional electrode permits the inclusion of ancillary tuning criteria and two particular cases are pursued here. To wit, we now consider tuning the modes to a specific target frequency or, alternatively, tuning the modes to degeneracy with the smallest maximum bias potential. Both of these scenarios can be motivated by system design constraints. Since an extra degree of freedom has been added ($n_e = 3$) we also increment the number of experiments for fitting the model parameters to $n_{\text{exp}} = 4$. Each experiment still generates frequency response data extending from 4385 Hz to 4445 Hz with 0.5 Hz resolution ($m_1 = m_2 = m_3 = m_4 = 121$, $n_R = 1$). There are 27 parameters to identify in (7) for which the frequency response data imposes 484 constraints.

The data sets are generated at the following bias potentials

$$[\delta v_{1,1}, \delta v_{1,2}, \delta v_{1,3}] = [0, 0, 0] \quad (19)$$
$$[\delta v_{2,1}, \delta v_{2,2}, \delta v_{2,3}] = [1, 0, 0] \quad (20)$$
$$[\delta v_{3,1}, \delta v_{3,2}, \delta v_{3,3}] = [0, 1, 0] \quad (21)$$
$$[\delta v_{4,1}, \delta v_{4,2}, \delta v_{4,3}] = [0, 0, 1]. \quad (22)$$

The frequency response of the identified model versus the data is shown in Fig. 11.

Once the model is in hand, we can tune the modal frequencies to a desired target, denoted ω_0, by solving

$$\begin{aligned} \text{min:} &\quad \gamma \\ \text{subject to:} &\quad \begin{bmatrix} \gamma I & Q^* \\ Q & \gamma I \end{bmatrix} \geq 0, \\ &\quad v_p^2 \geq 0, \, p = 1, \ldots, n_e, \end{aligned} \quad (23)$$

where

$$Q := \omega_0^2 M - \left(K_0 + \sum_{p=1}^{n_e} K_p v_p^2 \right).$$

For example, if $\omega_0 = 4430$ Hz, and $\omega_0 = 4435$ Hz, then (23) applied to the model in Fig. 11 yields

$$\omega_0 = 4430 \, \text{Hz} \rightarrow [\delta v_1, \delta v_2, \delta v_3] = [1.97, 4.38, -0.0412],$$
$$\omega_0 = 4435 \, \text{Hz} \rightarrow [\delta v_1, \delta v_2, \delta v_3] = [9.22, 4.48, 5.36].$$

Figure 12 shows the empirical data and model frequency frequency response obtained at these bias points.

An alternative to tuning the modal frequencies to a particular target frequency is to determine the smallest bias potential
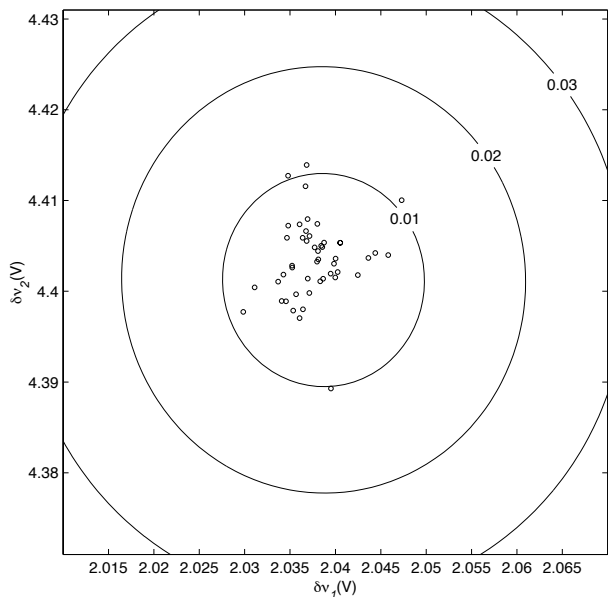
Fig. 10. The results of a second iteration of the algorithm in which new models are identified at the biases represented in Fig. 9. A second iteration gives satisfactory tuning results with the model that assumes input dynamics.
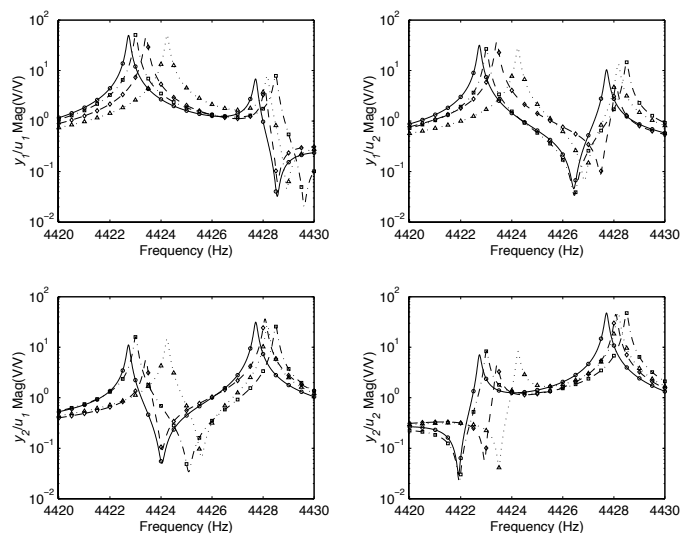

Fig. 11. Empirical frequency response of the sensor at the set of biases given in (19) thru (22) compared to the frequency response of the model fit to this data by solving (7). The circles, diamonds, triangles, and squares correspond to the data generated at (19), (20), (21), and (22), respectively.

magnitude that yields a tuned sensor. This problem is solved by reducing $\nu_{\max}$ in (14) until $\min \gamma > \varepsilon > 0$, where ε is a small positive parameter that represents a modicum of modal frequency detuning. This alternative scheme yields

$$[\delta\nu_1,\ \delta\nu_2,\ \delta\nu_3] = [-2.47,\ 4.30,\ -3.97],$$

corresponding to a tuned frequency of 4425.085 Hz. The empirical frsp is also shown in Fig. 12 when the sensor is tested at this bias point.

IV. CONCLUSION

As the fabrication processes for MEMS vibratory gyros continues to improve and produce devices with ever higher quality
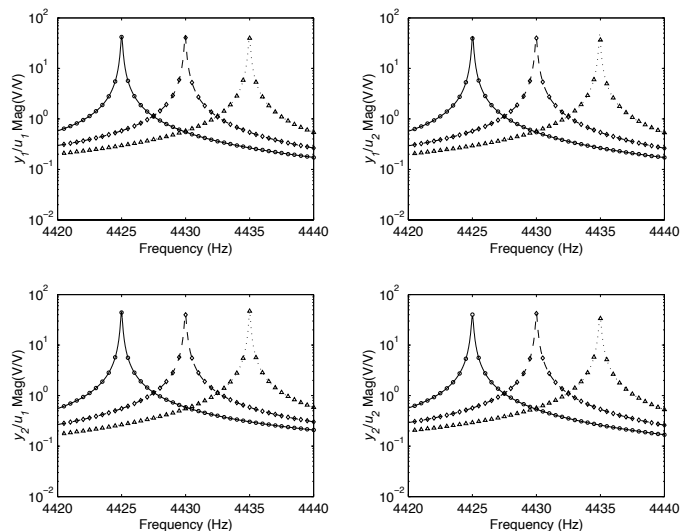

Fig. 12. Empirical frequency responses of the sensor when tuned to the target frequencies 4430 Hz and 4435 Hz. The data are represented by the diamonds and triangles. Also shown is the sensor frequency response of the tuned system that results from minimizing the maximum tuning potentials. The modes are tuned to 4425.085 Hz and the data are represented by circles.

factors, the degree to which the sensor dynamics can be tuned will define the sensor's ultimate performance. This paper has introduced and successfully applied a systematic method for tuning the modal frequencies of vibratory gyros.

REFERENCES

[1] Adams, S. D., Bertsch, F. M., Shaw, K. A., and MacDonald, N. C., "Independent tuning of linear and nonlinear stiffness coefficients," *Journal of Micromechanical Systems*, Jun. 1998, Vol. 7, No. 2, pp. 172-180.

[2] Bae, S. Y., Hayworth, K. J., Yee, K. Y., Shcheglov, K., and Wiberg, D. V., "High performance MEMS micro-gyroscope," *Proc. SPIE Vol. 4755*, Courtis, B, et. al, Ed., May 2002, pp. 316–24.

[3] Cabuz, C., Fukatsu, K., Hashimoto, H., Shoji, S., Kurabayashi, T., Minami, K., and Esashi, M. "Fine frequency tuning in resonant sensors," *Micro Electro Mechanical Systems, 1994, MEMS '94, Proceedings, IEEE Workshop*, 25-28 Jan. 1994, pp. 245 - 250.

[4] Chen, Y.-C. and M'Closkey, R. T., "Closed-loop identification of a microsensor," *Proceedings of the 42nd IEEE Conference on Decision and Control*, Maui, Hawaii, Dec. 2003, pp. 2632-2637.

[5] Fisher, D., Jue, D., Packard, A., and Poolla, K., "On the identification of high-order lightly-damped multivariable systems," Proceedings of the 1999 American Control Conference, San Diego, CA, Jun. 1999, vol.2, pp.848-853.

[6] Gallacher B.J., Burdess, J.S., Harris A.J., "Principles of a three-axis vibrating gyroscope," *IEEE Trans. Aerospace and Electronic Systems*, Oct. 2001, Vol. 37, No. 4, pp. 1333-1343.

[7] Joachim, D. and Lin, L., "Characterization of selective polysilicon deposition for MEMS resonator tuning," *Journal of Microelectromechanical Systems*, Apr. 2003, Vol. 12, No. 2, pp. 193-200.

[8] Juneau, T., Pisano, A.P., and Smith, J.H., "Dual axis operation of a micromachined rate gyroscope," *Intrntl. Conf. Solid State Sensors and Actuators, 1997*. June 1997, Vol. 2 , pp. 883–886.

[9] Kim, D.-J., and M'Closkey, R.T., "Real-time tuning of MEMS gyro dynamics," Proc. 2005 American Control Conf. (to appear).

[10] Lee, K. B., Yoon, J.-B., Kang, M.-S., Cho, Y.-H., Youn, S.-K., and Kim, C.-K., "A surface-micromachined tunable microgyroscope," *Proc. 1996 IEEE Conf. Emerging Technologies and Factory Automation*, Nov. 1996, Vol. 2 , pp. 498–502.

[11] Lee, K. B., and Cho, Y.-H., "Frequency tuning of a laterally driven microresonator using an electrostatic comb array of linearly varied length," *Solid State Sensors and Actuators, 1997. TRANSDUCERS '97 Chicago., 1997 International Conference* , Vol. 1 , 16-19 Jun. 1997 pp. 113 - 116.

[12] M'Closkey, R. T., Gibson, S., and Hui, J., "System identification of a MEMS gyroscope," *Journal of Dynamic Systems, Measurement, and Control, Transactions of the ASME*, Jun. 2001, vol. 123, No. 2, pp.201-210.

[13] Pourkamali, S., Hashimura, A., Adbolvand, R., Ho, G. K., Erbil, A. and Ayazi, F., "High-Q single crystal silicon HARPSS capacitive beam resonators with self-aligned sub-100-nm transduction gaps," *Journal of Microelectromechanical Systems*, Aug. 2003, Vol. 12, No. 4, pp. 487-496.

[14] Remtema, T. and Lin, L., "Active frequency tuning for micro resonators by localized thermal stressing effects," *Sensors and Actuators, Phys. A*, 2001, Vol. 91, pp. 326-332.

[15] Painter, C.C., and Shkel, A.M., "Active Structural Error Suppression in MEMS Vibratory Rate Integrating Gyroscopes," *IEEE Sensors J.*, Oct. 2003, Vol. 3, No. 5, pp. 595–606.

[16] Syms, R. R. A., "Electrothermal frequency tuning of folded and coupled vibrating micromechanical resonators," *Journal of Microelectromechanical Systems*, Jun. 1998, Vol. 7, No. 2, pp. 164-171.

[17] Tanaka, K., Mochida, K. Y., Sugimoto, S., Moriya, K., Hasegawa, T., Atsuchi, K., and Ohwada, K., "A micromachined vibrating gyroscope," *Sensors and Actuators, Phys. A*, 1995, Vol. 50, pp. 111-115.

[18] Tang, T. K., Gutierrez, R. C., Wilcox, J. Z., Stell, C., Vorperian, V., Calvet, R., Li, W. J., Charkaborty, I., Bartman, R., and Kaiser, W. J., "Silicon bulk micromachined vibratory gyroscope," *Solid-State Sensor and Actuator Workshop*, Hilton Head, SC, pp. 288-293, 1996.

[19] Yao, J. J. and MacDonald, N. C., "A micromachined, single-crystal silicon, tunable resonator," *J. Micromech. Microeng.*, 1995, vol. 5, pp. 257-264.